Frontiers of Information Technology & Electronic Engineering
www.jzus.zju.edu.cn; engineering.cae.cn; www.springerlink.com
ISSN 2095-9184 (print); ISSN 2095-9230 (online)
E-mail: jzus@zju.edu.cn

Long working distance portable smartphone microscopy for metallic mesh defect detection*

Zhengang LU†‡[1,2], Hongsheng QIN†[1,2], Jing LI[1,2,3], Ming SUN†[4], Jiubin TAN[1,2]

[1]*Center of Ultra-precision Optoelectronic Instrument Engineering, Harbin Institute of Technology, Harbin 150080, China*

[2]*Key Lab of Ultra-precision Intelligent Instrumentation (Harbin Institute of Technology), Ministry of Industry and Information Technology, Harbin 150080, China*

[3]*Institute of Materials, China Academy of Engineering Physics, Jiangyou 621907, China*

[4]*Visual Computing Center, King Abdullah University of Science and Technology, Thuwal 23955, Saudi Arabia*

†E-mail: luzhengang@hit.edu.cn; 21B901017@stu.hit.edu.cn; ming.sun@kaust.edu.sa

Received Nov. 13, 2024; Revision accepted Jan. 13, 2025; Crosschecked July 8, 2025

Abstract: Metallic mesh is a transparent electromagnetic shielding film with a fine metal line structure. However, in production preparation or actual use it can develop defects that affect the optoelectronic performance. The development of in situ non-destructive testing (NDT) devices for metallic mesh requires long working distances, reflective optical path design, and miniaturization. To address the limitations of existing smartphone microscopes, which feature short working distances and inadequate transmission imaging for industrial in situ inspection, we propose a novel long-working-distance reflective smartphone microscopy (LD-RSM) system. LD-RSM comprises a 4f optical imaging system with external optical components and a smartphone. This system uses a beam splitter to achieve reflective imaging with the illumination system and imaging system on the same side of the sample. It achieves an optical resolution of 4.92 μm and a working distance of up to 22.23 mm. Additionally, we introduce dual-prior weighted robust principal component analysis (DW-RPCA) for defect detection. This approach leverages spectral filter fusion and the Hough transform to model different defect types, which enhances the accuracy and efficiency of defect identification. Coupled with a double-threshold segmentation approach, the DW-RPCA method achieves a pixel-level defect detection accuracy (f-value) of 0.856 and 0.848 in square and circular metallic mesh datasets, respectively. Our work shows strong potential in the field of in situ industrial product inspection.

Key words: Smartphone microscope; Defect detection; Reflective portable imaging; Metallic mesh; Low-rank decomposition

https://doi.org/10.1631/FITEE.2401002 **CLC number:** TP391.41

1 Introduction

Recently, the rapid development of optoelectronic devices, including communication and medical devices and detectors, has enhanced human life significantly (Li MX et al., 2023). However, these devices emit a large amount of electromagnetic radiation, leading to electromagnetic interference (EMI). A well-designed metallic mesh can provide effective EMI shielding while maintaining transparency (Zhang et al., 2021; Liang et al., 2023). Metallic mesh is formed of periodic structures of thin metal films, and achieves high-frequency visible light transmission and low-frequency microwave cutoff by carefully selecting structural unit periods and line widths (Lu et al., 2024).

At present, there are many methods for the preparation of metallic mesh, such as photolithography coating (Qiu TF et al., 2022), the cracked template method (Zhu XY et al., 2021), nanoimprint

‡ Corresponding author

* Project supported by the National Natural Science Foundation of China (Nos. 61975046 and 62375068)

ORCID: Zhengang LU, https://orcid.org/0000-0001-6490-5819

lithography (Baracu et al., 2021), and direct writing (Li ZH et al., 2022). However, these mature technologies can still result in defects such as broken lines, metal deposition, and photoresist residue due to lithography process parameters and operator errors. In practical applications, metallic mesh can develop significant defects from scratches, impacts, and chemical erosion, which affect the performance of optoelectronic equipment. Defect detection in transparent electromagnetic shielding films during production is often limited to manual visual inspection, with a lack of adequate detection devices suitable for practical applications. Developing a miniaturized, cost-effective, portable device for microscopic defect detection could substantially improve the durability and performance of transparent electromagnetic shielding films.

Although the use of smartphone technologies in engineering detection remains relatively limited, significant progress has been made in developing portable diagnostic tools. These smartphone-based devices offer notable advantages, including high performance, low cost, miniaturization, and portability (Bui et al., 2023; Wang BF et al., 2023). Recent studies have documented various applications for these microscopes, demonstrating their broad utility (Ahmed et al., 2023; Zheng et al., 2023; Huang BX et al., 2024). Smartphone microscopes are capable of identifying white blood cells (Janev et al., 2023), imaging fresh tissue (Zhu WB et al., 2020), and measuring environmental lead (Pb) content (Lai et al., 2022). Most of these devices are designed as transmitted light microscopy systems, which are commonly used in biological and medical imaging. In this configuration, samples are positioned between the illumination and imaging systems, allowing light to pass through the sample.

The capacity to observe opaque objects is one of the significant extensions provided by the development of reflected light microscopy on smartphone-based platforms (Kim and Lee, 2023). However, the short working distance of most existing smartphone microscopes (typically ≤ 5 mm) (Kheireddine et al., 2019; Lee et al., 2021; Rabha et al., 2022a) poses a significant challenge for nondestructive detection during displacement scanning. To overcome this limitation, we introduce a reflective smartphone microscope with an extended working distance of 22.23 mm, which is engineered explicitly for the detection of defects in large-scale micro- and nanostructures. This advancement opens up new possibilities for industrial inspection applications using smartphone-based microscopy.

On the software side, detecting defects in structures like metallic mesh represents a significant challenge due to the intricate textures and diverse nature of potential defects. Traditionally, these precision devices undergo manual visual inspections during production—a labor-intensive process that underscores the need for a robust and systematic inspection framework. Defect detection in periodic texture structures, such as fabrics, remains a focal research area within defect detection. Researchers have developed several fabric defect detection algorithms using approaches such as the spectral method (Sakhare et al., 2015), statistical method (Alper Selver et al., 2014), modeling method (Zhou J et al., 2017), and deep learning method (Jing et al., 2022; Zhou CF et al., 2023). However, each method has its limitations.

Spectral methods often struggle with accuracy when detecting minor defects due to filter sensitivity. Statistical methods, on the other hand, tend to overlook global information and are computationally intensive. Although promising, deep learning algorithms require extensive datasets that are frequently unavailable in industrial settings, leading to compromised accuracy. Recently, defect detection algorithms based on low-rank decomposition models have garnered significant attention as a potential avenue for future research (Li W et al., 2024). These algorithms decompose images into low-rank (background), sparse (defect), and noise components (Candés et al., 2011). Ji et al. (2020) proposed a weighted low-rank and Laplace regularization approach to enhance defect-background separation, although its effectiveness is limited due to the use of Gabor features. Liu and Li (2022) advanced the field by introducing structural constraints in robust principal component analysis (RPCA), incorporating noise terms and defect priors, and leveraging spatial connections and 8D texture features for better defect detection. Bao et al. (2022) developed a method called PTVLR, which uses the structural similarity (SSIM) index as prior information. However, these approaches often fall short in accuracy, are time-consuming when extracting defect information from metallic mesh, and result in suboptimal

detection efficiency. In this paper, we introduce an enhanced low-rank decomposition model, dual-prior weighted robust principal component analysis (DW-RPCA), which is based on spectral filter fusion and the Hough transform. This model extracts prior defect information in metallic mesh and guides accurate low-rank decomposition. Furthermore, we employ a robotic arm for image scanning across the field of view, enabling comprehensive detection of defects in metallic mesh. When integrated with our miniaturized portable smartphone microscope (LD-RSM), this system markedly enhances the detection of defects in large-scale micro- and nanostructures, offering significant contributions to the field of industrial inspection. This work exemplifies a notable advancement in the synergy of hardware development and algorithmic innovation, improves inspection capabilities for metallic mesh defects, and paves the way for broader applications in industrial quality control.

2 Methodology

2.1 Smartphone microscope for industrial defect detection

Fig. 1 illustrates the prototyping of the LD-RSM system for industrial defect detection. This system is engineered to meet the demands of real-time, in situ defect detection, and incorporates a reflective optical path and extended working distance. The simplicity of its optical design not only ensures ease of production and deployment, but also contributes to its robust performance. LD-RSM integrates critical components, including imaging optics, illumination optoelectronics, and a mechanical structure for attachment to a robotic arm flange, all housed in a durable, three-dimensional (3D)-printed casing. The optical design of the present imaging system is depicted in Fig. 2a and is discussed in detail in Section 2.2. A monochromatic high-power coaxial point light source at a wavelength of 550 nm serves as LD-RSM's illumination, effectively minimizing the impact of chromatic aberration on imaging quality. Components are securely mounted within a housing that is fabricated by a fused-deposition modeling (FDM) 3D printer (model Raise N2). An optical clamping device secures industrial samples, ensuring stability during inspections. A 3D rendering of the LD-RSM system is presented in Fig. 2b, and the prototype of the developed microscopic system is showcased in Fig. 2c.

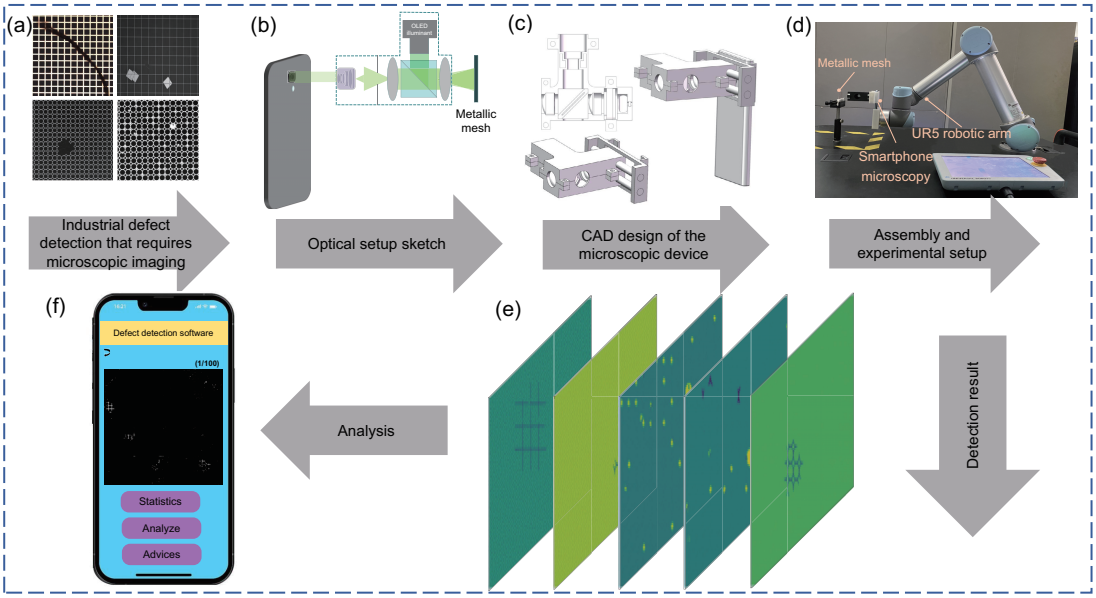

Fig. 1 Schematic of the rapid prototyping of the LD-RSM system: (a) microscopic imaging aids the in situ defect detection needs of metallic mesh; (b) optical setup (LD-RSM) sketch; (c) three-dimensional design of the microscopic device (LD-RSM) by computer-aided design (CAD); (d) assembly and experimental setup including robotic arm, LD-RSM, and metallic mesh samples; (e) defect detection results of LD-RSM-acquired images using dual-prior weighted robust principal component analysis (DW-RPCA); (f) defect detection software displays the detection results and allows for defect statistics, analysis, and advice

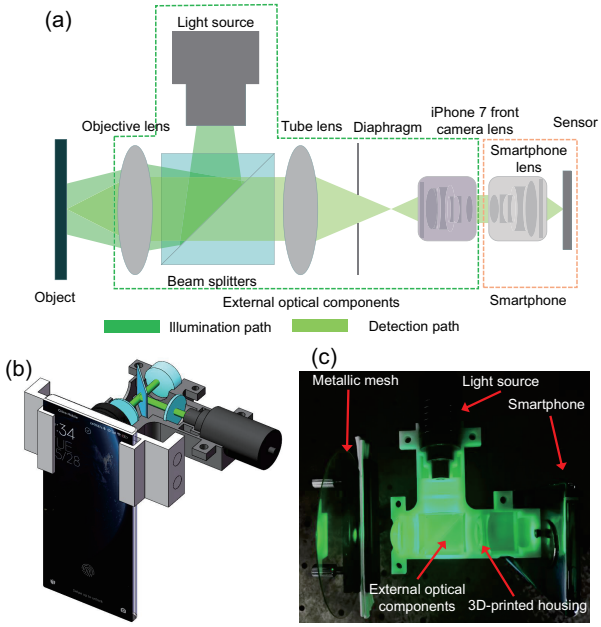

Fig. 2 Design and fabrication of the LD-RSM system: (a) schematic of a 4*f* optical configuration; (b) 3D rendering of the LD-RSM system; (c) prototype of the developed microscopic system

2.2 Imaging system design

There are two conventional approaches to configuring a microscopic setup on a smartphone: 3*f* and 4*f* imaging systems (Rabha et al., 2022b). In the 3*f* configuration, an external lens is mounted directly to the outside of the camera module of the smartphone to form a finite conjugate system. The external lens functions as the objective lens, and the smartphone's built-in set of lenses functions as the imaging system's tube lens. The sample is positioned at the focal plane of the objective lens. After the sample passes through the objective and tube lenses, the optical field is captured on the smartphone sensor. Given the small focal length of the smartphone lens (typically only a few millimeters), the external lens must have a similar small focal length to achieve greater magnification for microscopic imaging. However, due to its low magnification capability and the constraints imposed by the pixel pitch of the smartphone sensor, the setup often struggles with limited resolution and field of view, making it less suitable for practical industrial inspection.

To develop a high-quality, cost-effective optical system, we opt for the 4*f* imaging configuration for LD-RSM. This setup includes two large-focal-length lenses, a large-diameter lens as the objective, and a tube lens, along with a beam splitter, diaphragm, and light source, making it ideal for in situ imaging measurements of metallic mesh. The imaging principle is illustrated in Fig. 2a. Both the illumination and imaging optical paths are aligned on the same side of the sample to enable imaging measurements during equipment servicing without disassembly. Light from the source first passes through a beam splitter, which directs the reflected light onto the sample via the objective lens. The sample is placed at the focal plane of the objective lens. The reflected light carrying sample information then passes through the objective lens and the tube lens, forming an image on the focal plane of the tube lens. This image is then transferred to the smartphone camera module through a relay lens and captured on the camera sensor.

The imaging system employs a Redmi K30 Ultra smartphone (Xiaomi Inc., Beijing, China) equipped with a Sony IMX582 CMOS sensor (64-megapixel with a pixel size of 0.8 μm). The built-in lens of the smartphone features a focal length of 5.43 mm. Because the imaging focal length of the smartphone camera module is only 5.43 mm, the focal length of the relay lens cannot be too large considering the magnification of the system. The relay lens used here is derived from the iPhone 7 front camera module, which offers an imaging focal length of 2.87 mm and a numerical aperture (NA) of 0.23. Compared with the widely used ball lens and achromatic objective lens, a better imaging effect can be obtained by using the smartphone lens set.

The LD-RSM system requires placing the sample at the focal plane of the objective lens, where the focal length of the objective lens is crucial for determining the working distance. In this study, the objective lens is an achromatic double-glued lens from Edmund, with a focal length of 30 mm, a diameter of 25 mm, and an NA of 0.38. A long working distance of 22.23 mm is realized. The tube lens is integral for converged imaging, achieves adequate magnification, and maintains a compact form factor for the external device. We use an Edmund plano-convex lens with a focal length of 40 mm and a diameter of 25 mm. LD-RSM uses light from the transmitted portion of the beam splitter to image the sample, and the reflected portion is used for sample illumination. The Edmund beam splitter has a size of 35 mm × 35 mm

and a reflectance-to-transmittance ratio of 50/50.

2.3 Imaging acquisition and transmission

In this study, we employ the UR5 robotic arm to execute a programmed scanning sequence aimed at capturing images of metallic mesh within a defined area. The tool flange of the UR5 arm, equipped with four M6 threaded holes, facilitates the attachment of the LD-RSM device. We design a mechanical structure, as illustrated in Fig. 3a, based on the parameters of the UR5 arm's tool flange, using SolidWorks software (Onwubolu, 2017). This structure effectively connects LD-RSM to the UR5 arm and provides stable support for the scanning operation. The scanning protocol, depicted in Fig. 3b, is developed using the PolyScope programming environment. The UR5 robotic arm, carrying LD-RSM, autonomously scans the designated area of the metallic mesh in an S-pattern, systematically capturing images. To mitigate the risk of missed defect detection due to potential motion errors of the arm, we incorporate a degree of image redundancy in which the UR5 arm advances in 500 μm increments with each node.

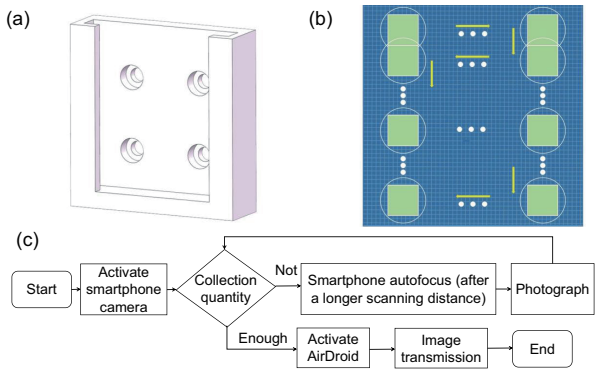

Fig. 3 Image acquisition and transmission strategies: (a) fixed mechanics for the UR5 arm and LD-RSM; (b) UR5 robotic arm scanning program; (c) LD-RSM script for automatic image acquisition and transmission

The control flow of the script program is shown in Fig. 3c. The automatic image acquisition and transmission of LD-RSM begins with the activation of the smartphone camera, then the number of images to be captured is determined, and the smartphone auto-focus (after a longer scanning distance) and photograph operations are performed cyclically. It should be noted that the parallelism between the sample and the LD-RSM imaging surface is high. It is found that the smartphone needs only initial focusing during the short-distance scanning process. After scanning a long distance, LD-RSM completes re-focusing, that is, through the smartphone's autofocusing function. Therefore, to ensure the imaging quality, we stay at each frame for 2 s to provide enough time for the auto-focusing process. Next, when the required number of images is met, the AirDroid software (Huang TY et al., 2015) is used to transmit the images.

2.4 Low-rank decomposition defect detection based on spectral filter fusion and the Hough transform

The defects that affect the photoelectric performance of metallic mesh fall into two categories: broken line and block defects. Based on the characteristics of these two types of defects, we propose DW-RPCA for metallic mesh defect detection. The proposed overall DW-RPCA detection process is shown in Fig. 4, which is composed mainly of three parts: prior information extraction, RPCA, and threshold segmentation.

In the prior information extraction phase, spectral and Hough priors are designed for defects of square metallic mesh and circular metallic mesh. These priors guide the low-rank decomposition process. As shown in Fig. 4, we use the Fourier transform to obtain the spectrogram whose frequency gradually increases from the center to the periphery. In this study, three square low-pass filters f_1, f_2, and f_3 are designed, and the side lengths of the square low-pass filters are 10, 20, and 40, respectively. These filters are applied to the spectrogram obtained previously. The Fourier inverse transform is then performed on the filtered spectrogram to obtain F_1, F_2, and F_3.

We use a linear combination to fuse the images obtained after filtering with three different filter sizes:

$$P_{\text{spectral}} = k_1 F_3 + k_2(F_1 + F_2) - k_3(F_2 - F_1), \tag{1}$$

where k_1, k_2, and k_3 are 0.8, 0.2, and 0.3, respectively. Then, the spectral prior about block defects is obtained by binarizing the resulting fusion map P_{spectral}.

RPCA and optimized RPCA-based models have difficulty in identifying a large range of multi-period

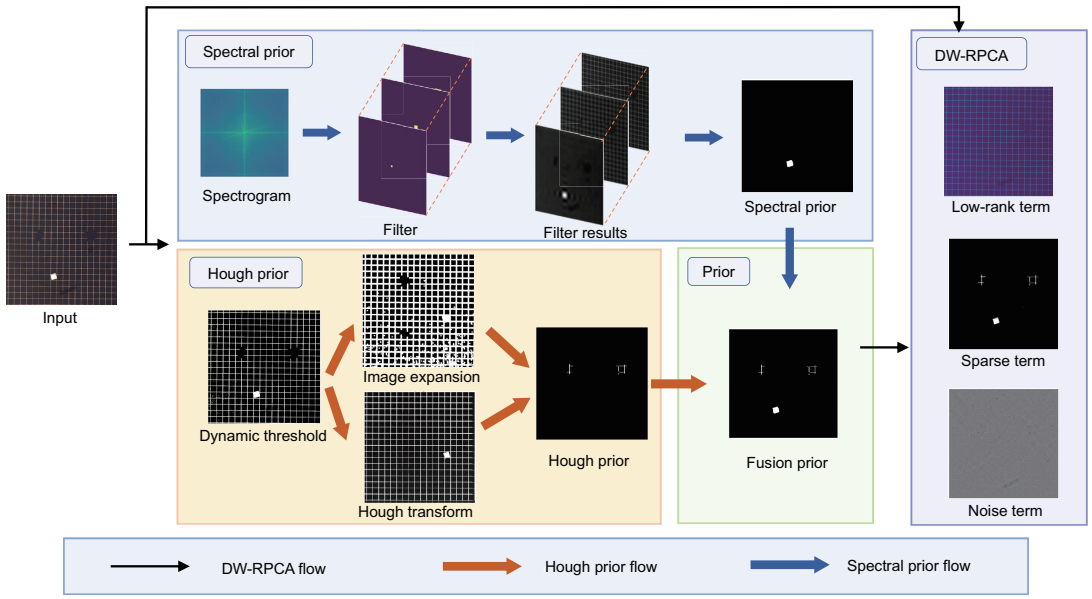

Fig. 4 Overall dual-prior weighted robust principal component analysis (DW-RPCA) detection process

broken line defects because these defects no longer satisfy the sparsity property. The Hough transform converts an image into a parameter space, which in turn maps the line or circle to be recognized to a point on the parameter space, thus transforming the problem of detecting shapes into a problem of peak point statistics. Therefore, for broken line defects, DW-RPCA introduces the Hough prior, as shown in Fig. 4, where the input image is first binarized using the dynamic thresholding algorithm, and the binarized image is then subjected to both image expansion and Hough transform detection. It should be noted that the Hough transform recognizes and converts the same line segment or circle into a complete line or circle in the image space. The result of the image expansion operation acts as a mask that prevents the complete line after broken line completion from being slightly shifted and incorrectly recognized as the defect. Eventually, the two are differentiated to obtain the final Hough prior result P_{hough}. In DW-RPCA, Hough prior P_{hough} and spectral prior P_{spectral} are fused to obtain the fusion prior P, which is used to guide the decomposition process in the sparse part, ensuring the accurate extraction of defects. The model is as follows:

$$\begin{aligned}&\min_{\boldsymbol{A},\boldsymbol{E}}\left(\|\boldsymbol{A}\|_*+\lambda\|\boldsymbol{W}\odot\boldsymbol{E}\|_1+\frac{\beta}{2}\|\boldsymbol{N}\|_{\mathrm{F}}^2\right)\\&\text{s.t. }\boldsymbol{I}=\boldsymbol{A}+\boldsymbol{E}+\boldsymbol{N},\end{aligned}\tag{2}$$

where $\boldsymbol{I},\boldsymbol{A},\boldsymbol{E}$, and $\boldsymbol{N}\in\mathbb{R}^{d\times d}$ are the input image, background matrix, defect matrix, and noise matrix, respectively. $\boldsymbol{W}\in\mathbb{R}^{d\times d}=\exp(-\boldsymbol{P})$ is the weight matrix. $\|\boldsymbol{A}\|_*=\mathrm{Tr}\left((\boldsymbol{A}^{\mathrm{T}}\boldsymbol{A})^{1/2}\right)$ denotes the nuclear norm of the low-rank matrix $\boldsymbol{A}$. $\|\boldsymbol{E}\|_1$ represents the 1-norm of the sparse matrix $\boldsymbol{E}$. $\|\boldsymbol{N}\|_{\mathrm{F}}^2$ is the Frobenius norm of the noise term $\boldsymbol{N}$. $\odot$ is the Hadamard product, and parameters λ and β are weights of different terms.

The Lagrangian function of the model is constructed as follows:

$$\begin{aligned}&\min_{\boldsymbol{A},\boldsymbol{E},\boldsymbol{N},\boldsymbol{Y},\mu}L(\boldsymbol{A},\boldsymbol{E},\boldsymbol{N},\boldsymbol{Y},\mu)\\&=\|\boldsymbol{A}\|_*+\lambda\|\boldsymbol{W}\odot\boldsymbol{E}\|_1+\frac{\beta}{2}\|\boldsymbol{N}\|_{\mathrm{F}}^2\\&+\langle\boldsymbol{Y},\boldsymbol{I}-\boldsymbol{A}-\boldsymbol{E}-\boldsymbol{N}\rangle+\frac{\mu}{2}\|\boldsymbol{I}-\boldsymbol{A}-\boldsymbol{E}-\boldsymbol{N}\|_{\mathrm{F}}^2,\end{aligned}\tag{3}$$

where μ is the penalty factor.

Using the alternating direction method of multipliers (ADMM) (Qiu JF et al., 2016) to solve the above equation, the specific solution procedure after introducing the prior information and adding the weight matrix is as follows:

$$\begin{aligned}\boldsymbol{E}_{k+1}&=\arg\min L\left(\boldsymbol{A}_k,\boldsymbol{E},\boldsymbol{N}_k,\boldsymbol{Y}_k,\mu_k\right)\\&=\arg\min_{\boldsymbol{E}}\left(\frac{\lambda}{\mu_k}\|\boldsymbol{W}\odot\boldsymbol{E}\|_1+\frac{1}{2}\|\boldsymbol{E}-\boldsymbol{X}_{\boldsymbol{E}}\|_{\mathrm{F}}^2\right),\end{aligned}\tag{4}$$

where $\boldsymbol{X}_{\boldsymbol{E}}=\boldsymbol{I}-\boldsymbol{A}_k-\boldsymbol{N}_k+\boldsymbol{Y}_k/\mu_k$. The L1-norm optimization problem with weight matrices can be

transformed into an operation between individual elements:

$$\begin{aligned} E_{k+1}(i,j) &= S_{\varepsilon(i,j)}\left(X(i,j)\right) \\ &= \operatorname{sgn}\left(X(i,j)\right)\cdot\max\Big[\operatorname{abs}\left(X(i,j)\right)-\varepsilon(i,j),\,0\Big], \end{aligned} \tag{5}$$

where $\varepsilon(i,j)=\lambda W(i,j)/\mu_k$, and S_ε denotes the soft-threshold operator, a solving procedure that replaces the dot-multiplication of matrices with operations between single elements. The overall flow of DW-RPCA is shown as Algorithm 1.

After DW-RPCA, defects need to be extracted by threshold segmentation. The gray value of broken line defects in the sparse part is typically less than zero, whereas block defects exhibit gray values greater than zero. Furthermore, the absolute gray value for broken line defects is relatively small, in contrast to the significantly larger absolute gray value of block defects. Based on these characteristics, defects are extracted using a double-threshold segmentation approach:

$$E(x,y)=\begin{cases} 255, & \text{if } E(x,y)\le t_1, \\ 255, & \text{if } E(x,y)>t_2, \\ 0, & \text{else}, \end{cases} \tag{6}$$

where t_1 and t_2 are thresholds, determined to be -5 and 50, respectively, by parameter scanning.

2.5 Sample preparation

The line widths of the metallic mesh are on the micron scale and are therefore processed using ultraviolet (UV) lithography, metal sputtering, and stripping processes (Wang HY et al., 2019). Initially, the mask design is prepared using L-Edit software, followed by mask fabrication using electron beam direct writing equipment. Subsequently, the process involves substrate pre-treatment, spin-coating of photoresist, pre-baking, UV exposure, post-baking, developing, rinsing, and drying. After the above process, the metallic mesh pattern on the mask plate is successfully transferred to the substrate photoresist (Lu et al., 2023). For the stripping process, the negative photoresist AR-N 4400-05 from ALLRESIST is employed. This photoresist offers high sensitivity and ease of removal, as well as high resolution of the contours of the photoresist pattern after development. Next, the metal layer is deposited on the adhesive film samples using a Technocor JCPF-2000A ultra-high vacuum dual-target magnetron sputtering machine, achieving a final thickness of approximately 100 nm. The metallic mesh is finalized using a stripping process, which involves immersion in an acetone solution combined with low-power ultrasonication and brush scrubbing. The samples are then thoroughly washed and dried to complete the fabrication process.

3 Results and discussion

3.1 Imaging system characterization

To obtain the best results from the LD-RSM system, an optimal distance of 22.23 mm is maintained between the sample and the external lens assembly edge. The optical magnification of LD-RSM is M1 (the ratio of the tube lens FL (focal length) = 40 mm to the objective lens FL = 30 mm) × M2 (the ratio of the phone's internal lens FL = 5.43 mm to the relay

Algorithm 1 ADMM flow for the DW-RPCA model

Require: metallic mesh image $\boldsymbol{I}$, defect prior $\boldsymbol{W}$, and parameters λ,β,ρ
Ensure: background matrix $\boldsymbol{A}$, defect matrix $\boldsymbol{E}$, and noise matrix $\boldsymbol{N}$
Initialize: $\boldsymbol{A}_0=\boldsymbol{E}_0=\boldsymbol{N}_0=\boldsymbol{Y}_0=\boldsymbol{0}$, maxstep = 10, $k=0$, $\mu_0=1/\|\boldsymbol{I}\|_2$, $\varepsilon=10^{-4}$, $\boldsymbol{W}=\exp(-\boldsymbol{P})$
while not converged or $k<$ maxstep **do**
  Update $\boldsymbol{E}$ by $\boldsymbol{E}_{k+1}=\arg\min_{\boldsymbol{E}}\Big(\frac{\lambda}{\mu_k}\|\boldsymbol{W}\odot\boldsymbol{E}\|_1+\frac{1}{2}\Big\|\boldsymbol{E}+\boldsymbol{A}_k+\boldsymbol{N}_k-\frac{\boldsymbol{Y}_k}{\mu_k}-\boldsymbol{I}\Big\|_{\mathrm{F}}^2\Big)$
  Update $\boldsymbol{N}$ by $\boldsymbol{N}_{k+1}=\frac{\mu_k(\boldsymbol{I}-\boldsymbol{A}_k-\boldsymbol{E}_{k+1})+\boldsymbol{Y}_k}{\beta+\mu_k}$
  Update $\boldsymbol{A}$ by $\boldsymbol{A}_{k+1}=\arg\min_{\boldsymbol{A}}\Big(\frac{1}{\mu_k}\|\boldsymbol{A}\|_*+\frac{1}{2}\Big\|\boldsymbol{A}+\boldsymbol{E}_{k+1}+\boldsymbol{N}_{k+1}-\frac{\boldsymbol{Y}_k}{\mu_k}-\boldsymbol{I}\Big\|_{\mathrm{F}}^2\Big)$
  // $\boldsymbol{A}$ can be solved via singular value decomposition
  Update $\boldsymbol{Y}$ by $\boldsymbol{Y}_{k+1}=\boldsymbol{Y}_k+\mu_k(\boldsymbol{I}-\boldsymbol{A}_{k+1}-\boldsymbol{E}_{k+1}-\boldsymbol{N}_{k+1})$
  Update μ by $\mu_{k+1}=\rho\mu_k$
  Check convergence: $\frac{\|\boldsymbol{I}-\boldsymbol{A}_{k+1}-\boldsymbol{E}_{k+1}-\boldsymbol{N}_{k+1}\|_{\mathrm{F}}^2}{\|\boldsymbol{I}\|_{\mathrm{F}}^2}<\varepsilon$
  $k=k+1$
end while

lens FL = 2.87 mm) = Mo = 2.52×. The phone has a screen size of 6.67 inches (diagonally) with an aspect ratio of 20:9, and its imaging sensor size is 1/1.7 inches (diagonally). Thus, the displayed image will have a digital magnification of Md = 18.0× on the phone's screen.

The resolution of LD-RSM has been characterized by imaging the 1951 USAF target. This is shown in Fig. 5a. Experimentally, under green light illumination, we measured a resolution of 4.92 μm, because it can resolve element 5 in group 6.

Due to the roughness of the sample surface, along with scattering and reflection within the optical system, LD-RSM has significant stray light interference compared to transmission microimaging systems. The presence of stray light in the LD-RSM system primarily arises from three sources. First, the uneven illumination from the LED source contributes to non-uniform light distribution. Second, scattering is induced by irregularities in the surface structure of the metallic mesh. Meanwhile, stray light is caused by reflections from multiple optical elements and the inner wall of the housing.

The diaphragm is situated in the focal plane to the left (near the tube lens). Note that the relay lens, adapted from an iPhone 7 front lens with a short 2.87 mm focal length, complicates precise diaphragm placement. Despite slight positional inaccuracies, this arrangement successfully reduces stray light and enhances imaging quality. To avoid degradation of image clarity from light reflecting off the shell and re-entering the imaging path, an opening is strategically placed in the transmitted path after the splitter. Figs. 5b and 5c compare the imaging results before and after the measures to suppress stray light. The imaging results show that the above improvement measures greatly reduce the impact of stray light on the system's imaging quality, and the imaging clarity is significantly improved.

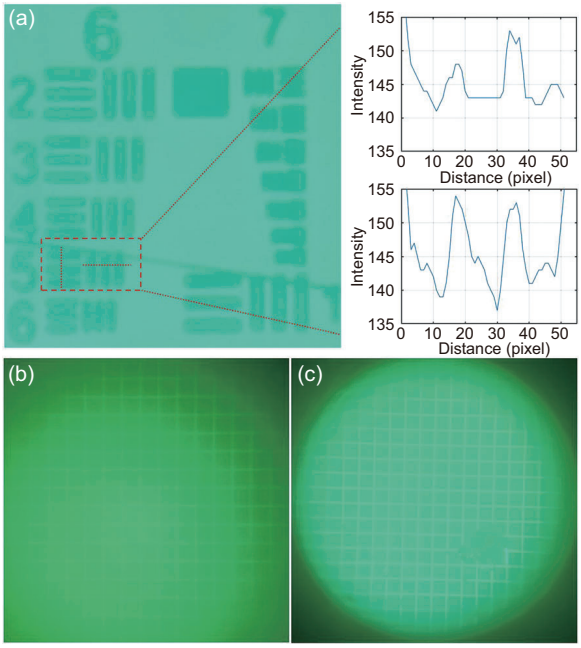

Fig. 5 Characterization of the LD-RSM system: (a) image of a USAF-1951 resolution test target acquired by LD-RSM; (b) imaging result before improvement; (c) imaging result after the measures to suppress stray light

3.2 Quantitative analysis of DW-RPCA by metallic mesh defect detection

To verify the advanced nature of DW-RPCA, we prepared metallic mesh datasets before the experiment and conducted a quantitative comparison with existing advanced models.

1. Metallic mesh datasets

As the core device of transparent conductive film and transparent electromagnetic shielding, the photoelectric performance of metallic mesh is limited by two types of defects: broken lines and block defects. Broken line defects are caused by wear and scratches during processing and application. The cause of block defects is the presence of metal residues due to improper operation or temperature during the photolithography process. To verify the performance of DW-RPCA, this study prepared the metallic mesh of square and circular structures. The square metallic mesh dataset and the circular metallic mesh dataset are two sets of 60 images containing broken lines, blocks, and mixed defects used by the laser confocal microscope OLYMPUS OLS5000. Labelme software (Russell et al., 2008) is used to label the ground truth. It should be pointed out that the resolution is configured to 256 × 256 pixels for standardization with existing defect datasets.

2. Evaluation metrics and parameter analysis

To quantitatively assess the state of the art of the model, true positive (TP), true negative (TN), false positive (FP), and false negative (FN) are introduced for evaluating the detection performance of the defect detection algorithms. From these values, we derive the following as evaluation metrics, which

are critical for performance assessment:

$$\begin{cases} \mathrm{TPR} = \dfrac{\mathrm{TP}}{\mathrm{FN}+\mathrm{TP}}, & \mathrm{FPR} = \dfrac{\mathrm{FP}}{\mathrm{FP}+\mathrm{TN}}, \\ \mathrm{PPV} = \dfrac{\mathrm{TP}}{\mathrm{FP}+\mathrm{TP}}, & \mathrm{NPV} = \dfrac{\mathrm{TN}}{\mathrm{TN}+\mathrm{FN}}, \end{cases} \tag{7}$$

$$f = \frac{(\gamma^2+1)\cdot \mathrm{TPR}\cdot \mathrm{PPV}}{\mathrm{TPR}+\gamma^2\cdot \mathrm{PPV}}, \tag{8}$$

where the value of f combines the true rate and the positive predictive value, and we set $\gamma = 1$.

In the DW-RPCA model, there are two weighting parameters λ and β. Using the gridded parameter scanning method, $\lambda = 0.11$ and $\beta = 0.003$ are determined in the square metallic mesh image set. We set $\lambda = 0.06$, $\beta = 0.004$ in the circular metallic mesh.

3. Comparative models

To validate the performance of DW-RPCA, we conduct comparisons with traditional defect detection algorithms, including PG-LSR (Cao et al., 2017), ID (Ng et al., 2014), WT (Imamoglu et al., 2013), PN-RPCA (Cao et al., 2016), and SOMC (Li CL et al., 2019).

PG-LSR (Cao et al., 2017) calculates an irregularity map by prior knowledge-guided least-squares regression after extracting feature vectors for each block of the fabric image. Defective regions are obtained through automatic thresholding. The ID (Ng et al., 2014) method models a defective fabric image as a superposition of cartoon and texture structures. It employs the total variation and a semi-norm in the negative Sobolev space to regularize these two components. This image decomposition process is optimized by maximizing the correlation between a defect-free reference fabric image and the texture structure of the testing image. WT (Imamoglu et al., 2013) creates feature maps by inverse wavelet transformation on multi-level decompositions. Each feature map captures band-pass local information at different frequency bandwidths. The final saliency map is generated by combining local and global saliency maps. PN-RPCA (Cao et al., 2016) incorporates a noise term and defect prior based on RPCA. The defect prior guides matrix recovery, enabling accurate identification of sparse terms as fabric defects. SOMC (Li CL et al., 2019) first generates a second-order multi-channel feature descriptor inspired by the P-type ganglion cell coding in the primate retina. Using a joint low-rank decomposition framework, the fabric image is decomposed into background and salient defect components.

4. Experiments on the metallic mesh dataset of DW-RPCA

Validation is conducted using the square metallic mesh defect image dataset, with representative results shown in Fig. 6. Quantitative comparisons of the measurement metrics of different methods are listed in Table 1. PG-LSR and WT struggle to detect broken line defects. PG-LSR integrates local priors with the global feature space structure, making it sensitive to block defects. Although it has a low false detection rate, it fails to identify more minor defects. WT has high FPR and low PPV due to its ability to detect block defects but with

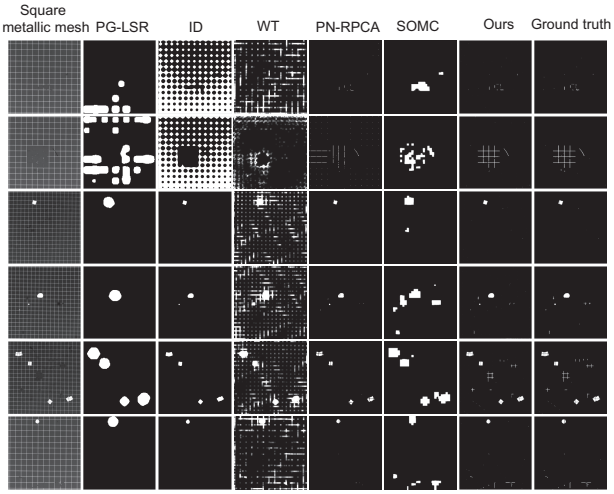

Fig. 6 Visual comparisons with five representative methods on the square metallic mesh dataset

Table 1 Quantitative comparisons of the square metallic mesh dataset

Defect	TPR	FPR	PPV	NPV	f	Method
Broken	0.3909	0.1565	0.0086	0.9966	0.0168	PG-LSR
	0.1821	0.4680	0.0009	0.9939	0.0019	ID
	0.3413	0.2579	0.0046	0.9956	0.0091	WT
	0.5097	0.0011	0.7423	0.9974	0.6009	PN-RPCA
	0.6905	0.0298	0.0730	0.9980	0.1274	SOMC
	0.8158	**0.0003**	**0.8860**	**0.9995**	**0.8480**	Ours
Block	0.9227	0.0237	0.1372	**0.9997**	0.2356	PG-LSR
	0.8667	0.0445	0.8148	0.9994	0.8023	ID
	0.9456	0.2592	0.0172	**0.9997**	0.0334	WT
	0.7768	**0.0001**	**0.9892**	0.9989	0.8651	PN-RPCA
	0.9713	0.0252	0.1429	0.9995	0.2464	SOMC
	0.8772	0.0004	0.8769	0.9995	**0.8753**	Ours
Mixed	0.5720	0.0365	0.1142	0.9972	0.1886	PG-LSR
	0.5388	0.0918	0.7114	0.9963	0.5783	ID
	0.5750	0.2441	0.0218	0.9950	0.0412	WT
	0.3667	**0.0001**	**0.9841**	0.9943	0.5174	PN-RPCA
	0.8605	0.0441	0.1423	0.9986	0.2414	SOMC
	0.8157	0.0006	0.8815	**0.9989**	**0.8460**	Ours

The best results are in bold

significant noise. Similarly, ID fails to detect broken line defects and may misidentify other elements. PN-RPCA can basically detect broken wires and block defects, but it fails to detect mixed type defects, resulting in significant missed detections. Although FPR is low, TPR is poor. SOMC has a high TPR but a low f-number. This is because SOMC can detect defects, but the significant blocks are large, and it also misses mixed defects. In contrast, DW-RPCA demonstrates a clear advantage in detecting defects in square metallic mesh data.

Fig. 7 presents the comparison of defect detection methods for the circular metallic mesh dataset. PG-LSR can generally locate significant defects; however, defect characterization makes it difficult to classify defects. ID fails to detect broken line defects and small-sized block defects. WT can detect obvious defects, but it generates significant FPs due to noise. The inability of the 8D texture method in PN-RPCA to extract prior information about small-area block defects results in poor performance in detecting these defects. SOMC can detect most defects but struggles to distinguish between defect types. DW-RPCA can accurately localize and characterize defects, closely matching the ground truth. Quantitative comparisons of the metrics of different methods are listed in Table 2. It can be seen that PN-RPCA has advantages in FPR and PPV, but TPR and f value are not as good as the counterparts of DW-RPCA because the former has more missed detections. SOMC has a higher TPR but a lower PPV, whereas DW-RPCA offers comprehensive advantages across metrics.

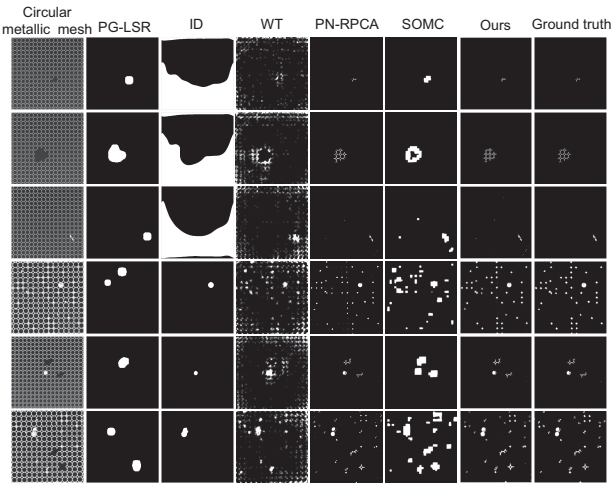

Fig. 7 Visual comparisons with five baseline methods on the circular metallic mesh dataset

Table 2 Quantitative comparisons of the circular metallic mesh dataset

Defect	TPR	FPR	PPV	NPV	f	Method
Broken	0.6159	0.0246	0.0539	0.9996	0.0983	PG-LSR
	0.1821	0.4680	0.0009	0.9939	0.0019	ID
	0.2466	0.1985	0.0049	0.9980	0.0096	WT
	0.4469	**0.0001**	**0.9382**	0.9975	0.6035	PN-RPCA
	0.9008	0.0219	0.1508	0.9993	0.2537	SOMC
	0.9564	0.0004	0.8089	**0.9998**	**0.8716**	Ours
Block	0.3350	0.0333	0.1110	0.9908	0.1360	PG-LSR
	0.8667	0.0445	0.8148	**0.9994**	0.8023	ID
	0.9629	0.2131	0.0512	0.9993	0.0948	WT
	0.6079	0.0066	**0.8365**	0.9946	0.6566	PN-RPCA
	0.7352	0.0414	0.1496	0.9958	0.2446	SOMC
	0.8479	**0.0019**	0.8095	0.9977	**0.8288**	Ours
Mixed	0.3015	0.0225	0.1294	0.9878	0.1618	PG-LSR
	0.5388	0.0918	0.7114	0.9963	0.5783	ID
	0.6424	0.2013	0.0815	0.9890	0.1409	WT
	0.3821	0.0069	**0.8526**	0.9832	0.5027	PN-RPCA
	0.7014	0.0586	0.2194	0.9897	0.3277	SOMC
	0.8514	**0.0025**	0.8489	**0.9974**	**0.8496**	Ours

The best results are in bold

The TPR-FPR scatter plot and f-value histogram are shown in Fig. 8. In the scatter plot, the upper-left corner is most desirable, indicating a higher TPR and a lower FPR, signifying superior defect detection performance by the algorithm. Higher values correlate with better performance in the f-value histogram.

The scatter distributions for PG-LSR, WT, ID, and SOMC are notably scattered and far from the vertical axis, which indicates marked underperformance compared to DW-RPCA. The scatter distributions of PN-RPCA, closer to the vertical axis,

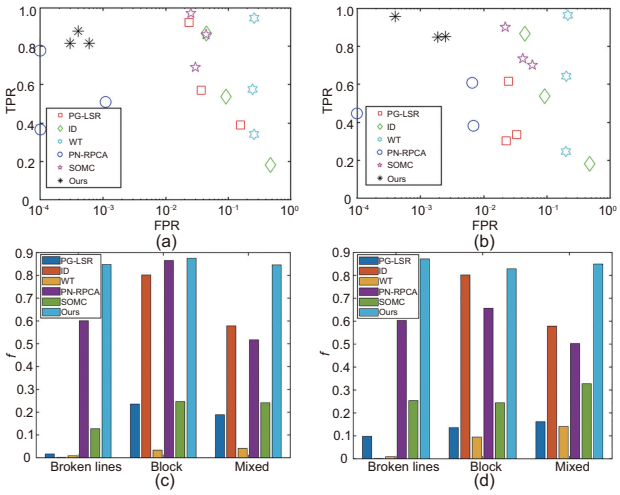

Fig. 8 TPR-FPR scatter plot of square metallic mesh (a) and circular metallic mesh (b), and f-value histogram of square metallic mesh (c) and circular metallic mesh (d)

suggest higher FPRs and worse TPRs compared to DW-RPCA. In the f-value histogram for the square and circular metallic meshes, PG-LSR, ID, WT, and SOMC perform poorly, PN-RPCA achieves good results, and DW-RPCA achieves an optimal f-value for all three types of defective image sets.

3.3 Experimental results of LD-RSM

Square metallic mesh and circular metallic mesh images are acquired by the proposed LD-RSM system to validate the performance of DW-RPCA. Note that ground truth is generally not available due to the large number and complexity of the actual collection scenarios. Fig. 9 shows the acquired images of the square metallic mesh and the circular metallic mesh with the comparison of multiple defect detection results. Columns 2–6 show the PG-LSR, ID, WT, PN-RPCA, and SOMC used for comparison with the DW-RPCA and prior information, as in columns 7 and 8, respectively. It can be found that PG-LSR has a certain detection effect. However, PG-LSR has a more severe misdetection phenomenon and is ineffective for the detection of defects with a small area. ID detects defects with a large-area misdetection, and we deem that the problem is caused by uneven light intensity and image noise. WT also fails to detect defects. PN-RPCA can generally detect defects. However, its performance on authentic images is not as good as before due to its insufficient anti-interference ability. SOMC can detect defects, but there are some FPs. DW-RPCA is robust to uneven illumination, noise, and other problems, and can realize fast and accurate detection for three types of defects of different sizes and shapes, effectively handling the misdetection and leakage issues.

DW-RPCA is used to detect defects in the acquired image of a specific region (2 mm × 2 mm) by LD-RSM. Fig. 10 shows the results of large metallic mesh defect detection. The results are accurate. This indicates that the refined metallic mesh defect detection system constructed in this study can realize the ultra-field-of-view range of specific areas of the metallic mesh, by scanning the image using the UR5 robotic arm and LD-RSM and then using DW-RPCA for fast and accurate detection.

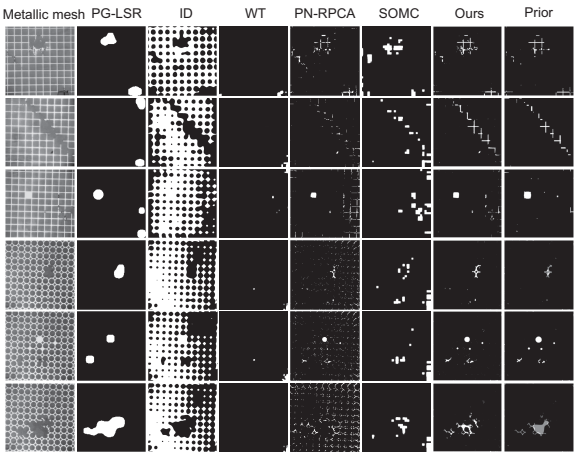

Fig. 9 Acquired images of square metallic mesh and circular metallic mesh with the comparison of multiple defect detection results

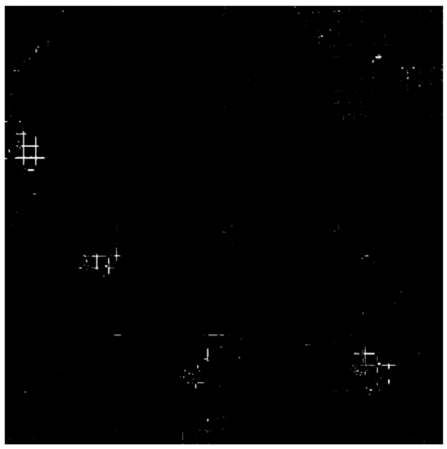

Fig. 10 Results of large metallic mesh (2 mm × 2 mm) defect detection

4 Conclusions

In this paper, a reflective portable imaging system (LD-RSM) is proposed to realize imaging of metallic mesh in the in situ state. The optical path structure, coupled with an external lens assembly and a smartphone camera module, enables the imaging system to achieve a working distance of 22.23 mm, meeting the requirements for nondestructive testing. The introduction of an aperture diaphragm and other stray light filtering designs effectively reduces the impact of stray light on the imaging system's quality. Experimental results show that the resolution of the reflective portable imaging system is 4.92 μm, and the magnification meets the imaging quality requirements of metallic mesh. A low-rank decomposition defect detection algorithm based on the fusion of spectral filtering and the

Hough transform (DW-RPCA) is also proposed to detect defects in square and circular metallic meshes. DW-RPCA has the best detection results compared to other methods, achieving an f-value of 0.856 for square metallic mesh and 0.848 for circular metallic mesh. Finally, the performances of LD-RSM and DW-RPCA are demonstrated in combination with a UR5 robotic arm to realize the ultra-field-of-view inspection of large-scale micro- and nanostructures. This provides a low-cost and efficient solution for industrial in situ inspection.

Contributors

Zhengang LU supervised and conceptualized the research, and contributed to methodology, validation, and writing. Hongsheng QIN handled investigation, visualization, formal analysis, and data curation. Jing LI worked on dataset preparation, software development, and data curation. Ming SUN contributed to writing and reviewing. Jiubin TAN provided supervision and reviewed the paper.

Conflict of interest

Zhengang LU and Jiubin TAN are a corresponding expert and an editorial board member of *Frontiers of Information Technology & Electronic Engineering*, respectively; they were not involved with the peer review process of this paper. All the authors declare that they have no conflict of interest.

Data availability

The data that support the findings of this study are available from the corresponding author upon reasonable request.

References

Ahmed I, Elsherif M, Ali M, et al., 2023. Photonic hydrogel for continuous glucose monitoring using smartphone readout. *Mater Des*, 231:112065. https://doi.org/10.1016/j.matdes.2023.112065

Alper Selver M, Avşar V, Özdemir H, 2014. Textural fabric defect detection using statistical texture transformations and gradient search. *J Text Inst*, 105(9):998-1007. https://doi.org/10.1080/00405000.2013.876154

Bao XY, Liang JZ, Xia YF, et al., 2022. Low-rank decomposition fabric defect detection based on prior and total variation regularization. *Visual Comput*, 38(8):2707-2721. https://doi.org/10.1007/s00371-021-02148-9

Baracu AM, Avram MA, Breazu C, et al., 2021. Silicon metalens fabrication from electron beam to UV-nanoimprint lithography. *Nanomaterials*, 11(9):2329. https://doi.org/10.3390/nano11092329

Bui TH, Thangavel B, Sharipov M, et al., 2023. Smartphone-based portable bio-chemical sensors: exploring recent advancements. *Chemosensors*, 11(9):468. https://doi.org/10.3390/chemosensors11090468

Candés EJ, Li XD, Ma Y, et al., 2011. Robust principal component analysis. *J ACM*, 58(3):1-37. https://doi.org/10.1145/1970392.1970395

Cao JJ, Wang NN, Zhang J, et al., 2016. Detection of varied defects in diverse fabric images via modified RPCA with noise term and defect prior. *Int J Cloth Sci Technol*, 28(4):516-529. https://doi.org/10.1108/IJCST-10-2015-0117

Cao JJ, Zhang J, Wen ZJ, et al., 2017. Fabric defect inspection using prior knowledge guided least squares regression. *Multim Tools Appl*, 76(3):4141-4157. https://doi.org/10.1007/s11042-015-3041-3

Huang BX, Kang L, Tsang VTC, et al., 2024. Deep learning-assisted smartphone-based quantitative microscopy for label-free peripheral blood smear analysis. *Biomed Opt Expr*, 15(4):2636-2651. https://doi.org/10.1364/BOE.511384

Huang TY, Wang HH, Peng CL, et al., 2015. A new remote desktop approach with mobile devices: design and implementation. *Lect Notes Electr Eng*, 331:305-321. https://doi.org/10.1007/978-94-017-9618-7_29

Imamoglu N, Lin WS, Fang YM, 2013. A saliency detection model using low-level features based on wavelet transform. *IEEE Trans Multim*, 15(1):96-105. https://doi.org/10.1109/TMM.2012.2225034

Janev A, Kang JS, Park SY, 2023. A smartphone integrated paper (SIP)-based platform for rapid and on-site screening of urinary tract infections. *Sens Actuat B Chem*, 382:133498. https://doi.org/10.1016/j.snb.2023.133498

Ji X, Liang JZ, Di L, et al., 2020. Fabric defect fetection via weighted low-rank decomposition and Laplacian regularization. *J Eng Fibers Fabr*, 15:1-14. https://doi.org/10.1177/1558925020957654

Jing JF, Wang Z, Rätsch M, et al., 2022. Mobile-Unet: an efficient convolutional neural network for fabric defect detection. *Text Res J*, 92(1-2):30-42.

Kheireddine S, Perumal AS, Smith ZJ, et al., 2019. Dual-phone illumination-imaging system for high resolution and large field of view multi-modal microscopy. *Lab Chip*, 19(5):825-836. https://doi.org/10.1039/c8lc00995c

Kim K, Lee WG, 2023. Portable, automated and deep-learning-enabled microscopy for smartphone-tethered optical platform towards remote homecare diagnostics: a review. *Small Methods*, 7(1):2200979. https://doi.org/10.1002/smtd.202200979

Lai WQ, Chang YF, Chou FN, et al., 2022. Portable FRET-based biosensor device for on-site lead detection. *Biosensors*, 12(3):157. https://doi.org/10.3390/bios12030157

Lee KC, Lee K, Jung J, et al., 2021. A smartphone-based Fourier ptychographic microscope using the display screen for illumination. *ACS Photon*, 8(5):1307-1315. https://doi.org/10.1021/acsphotonics.1c00350

Li CL, Liu CD, Gao GS, et al., 2019. Robust low-rank decomposition of multi-channel feature matrices for fabric defect detection. *Multim Tools Appl*, 78(6):7321-7339. https://doi.org/10.1007/s11042-018-6483-6

Li MX, Zarei M, Mohammadi K, et al., 2023. Silver meshes for record-performance transparent electromagnetic interference shielding. *ACS Appl Mater Interf*, 15(25):30591-30599. https://doi.org/10.1021/acsami.3c02088

Li W, Wang HY, Huo LZ, et al., 2024. Low-rank matrix recovery with total generalized variation for defending adversarial examples. *Front Inform Technol Electron Eng*, 25(3):432-445. https://doi.org/10.1631/FITEE.2300017

Li ZH, Li HK, Zhu XY, et al., 2022. Directly printed embedded metal mesh for flexible transparent electrode via liquid substrate electric-field-driven jet. *Adv Sci*, 9(14):2105331. https://doi.org/10.1002/advs.202105331

Liang YL, Huang XJ, Wen K, et al., 2023. Metal mesh-based infrared transparent EMI shielding window with balanced shielding properties over a wide frequency spectrum. *Appl Sci*, 13(8):4846. https://doi.org/10.3390/app13084846

Liu GH, Li F, 2022. Fabric defect detection based on low-rank decomposition with structural constraints. *Visual Comput*, 38(2):639-653. https://doi.org/10.1007/s00371-020-02040-y

Lu ZG, Zhang YL, Wang HY, et al., 2023. Transparent thermally tunable microwave absorber prototype based on patterned VO_2 film. *Engineering*, 29:198-206. https://doi.org/10.1016/j.eng.2022.10.005

Lu ZG, Cao ZB, Tan JB, 2024. A valid evaluation method for electromagnetic shielding efficiency of metallic mesh based on free-space reflection measurement. *IEEE Trans Instrum Meas*, 73:6002207. https://doi.org/10.1109/TIM.2023.3348888

Ng MK, Ngan HYT, Yuan XM, et al., 2014. Patterned fabric inspection and visualization by the method of image decomposition. *IEEE Trans Autom Sci Eng*, 11(3):943-947. https://doi.org/10.1109/TASE.2014.2314240

Onwubolu GC, 2017. Introduction to SolidWorks: a Comprehensive Guide with Applications in 3D Printing. CRC Press, Boca Raton, USA.

Qiu JF, Wu QH, Ding GR, et al., 2016. A survey of machine learning for big data processing. *EURASIP J Adv Signal Process*, 2016(1):67.

Qiu TF, Akinoglu EM, Luo B, et al., 2022. Nanosphere lithography: a versatile approach to develop transparent conductive films for optoelectronic applications. *Adv Mater*, 34(19):2103842. https://doi.org/10.1002/adma.202103842

Rabha D, Biswas S, Hatiboruah D, et al., 2022a. An affordable, handheld multimodal microscopic system with onboard cell morphology and counting features on a mobile device. *Analyst*, 147(12):2859-2869. https://doi.org/10.1039/d1an02317a

Rabha D, Rather MA, Mandal M, et al., 2022b. Programmable illumination smartphone microscopy (PISM): a multimodal imaging platform for biomedical applications. *Opt Laser Eng*, 151:106931. https://doi.org/10.1016/j.optlaseng.2021.106931

Russell BC, Torralba A, Murphy KP, et al., 2008. LabelMe: a database and web-based tool for image annotation. *Int J Comput Vis*, 77(1-3):157-173. https://doi.org/10.1007/s11263-007-0090-8

Sakhare K, Kulkarni A, Kumbhakarn M, et al., 2015. Spectral and spatial domain approach for fabric defect detection and classification. Int Conf on Industrial Instrumentation and Control, p.640-644.

Wang BF, Li YW, Zhou MF, et al., 2023. Smartphone-based platforms implementing microfluidic detection with image-based artificial intelligence. *Nat Commun*, 14(1):1341. https://doi.org/10.1038/s41467-023-36017-x

Wang HY, Ji CG, Zhang C, et al., 2019. Highly transparent and broadband electromagnetic interference shielding based on ultrathin doped Ag and conducting oxides hybrid film structures. *ACS Appl Mater Interf*, 11(12):11782-11791. https://doi.org/10.1021/acsami.9b00716

Zhang YL, Cao JX, Lu ZG, et al., 2021. Comprehensive evaluation factor of optoelectronic properties for transparent conductive metallic mesh films. *Front Inform Technol Electron Eng*, 22(11):1532-1540. https://doi.org/10.1631/FITEE.2000690

Zheng YH, Yin H, Zhou CX, et al., 2023. A hand-held platform for boar sperm viability diagnosis based on smartphone. *Biosensors*, 13(11):978. https://doi.org/10.3390/bios13110978

Zhou CF, Liu MQ, Zhang SL, et al., 2023. A graph-based two-stage classification network for mobile screen defect inspection. *Front Inform Technol Electron Eng*, 24(2):203-216. https://doi.org/10.1631/FITEE.2200524

Zhou J, Wang J, Bu HG, 2017. Fabric defect detection using a hybrid and complementary fractal feature vector and FCM-based novelty detector. *Fibres Text East Eur*, 25(6):46-52. https://doi.org/10.5604/01.3001.0010.5370

Zhu WB, Pirovano G, O'Neal PK, et al., 2020. Smartphone epifluorescence microscopy for cellular imaging of fresh tissue in low-resource settings. *Biomed Opt Expr*, 11(1):89-98. https://doi.org/10.1364/BOE.11.000089

Zhu XY, Liu MY, Qi XM, et al., 2021. Templateless, plating-free fabrication of flexible transparent electrodes with embedded silver mesh by electric-field-driven microscale 3D printing and hybrid hot embossing. *Adv Mater*, 33(21):2007772. https://doi.org/10.1002/adma.202007772